# MET.O.14

METEOROLOGICAL OFFICE
BOUNDARY LAYER RESEARCH BRANCH
TURBULENCE & DIFFUSION NOTE

T.D.N. No. 107

## A NUMERICAL STUDY OF RAPIDLY-ROTATING FLOW OVER SURFACE-MOUNTED OBSTACLES

by

P.J.Mason & R.I.Sykes

December 1978

LP

Submitted to JFM

DEC 78

# A numerical study of rapidly-rotating flow over surface-mounted obstacles

by

P.J. Mason & R.I. Sykes

Meteorological Office,

Bracknell,

Berkshire.

Abstract

Three-dimensional numerical integrations of the Navier-Stokes equations have been made for parameters corresponding to some previous laboratory studies of Taylor columns. The results help clarify the character of these flows and confirm previous ideas concerning the role played by inertial waves in flows which have been described as 'leaning Taylor columns'. The wavelike character is not obvious in laboratory studies due to viscous effects. Integrations in shallow domains indicate the validity of the assumptions of two-dimensionality for these flows.

## 1. Introduction

Previous work on transverse flow past obstacles in a rotating fluid has largely centred on the study of "Taylor columns". For sufficiently small values of Rossby number ($R = U/\Omega L$, where $U$ is the flow speed, $\Omega$ the rotation speed and $L$ a typical horizontal length) the rapid rotation constrains the motion about the obstacle to be two-dimensional (the Taylor-Proudman theorem: Proudman 1916, Taylor 1923). The flow past the object can then be divided into two regions separated by an imaginary cylinder with axis parallel to the axis of rotation, which circumscribes the object. Outside this cylinder (a 'Taylor column') the flow behaves as if it were encountering a solid cylinder. The exact conditions for a Taylor column to form have been discussed by Hide (1961) who proposed a criterion depending on the change in vorticity necessary for fluid filament to cross the object, compared with the voriticity of the basic flow. It follows thata a Taylor column should form when $\delta_h = \frac{h}{DR} \gg 1$ ($h$ is the height of the object and $D$ the depth of the fluid). This is the criterion for virtually no flow over the obstacle and should be distinguished from the criterion for the flow to be nearly two-dimensional. The axial scale of a disturbance with horizontal scale $L$ will be $L/R$ and thus we require $\delta_L = \frac{L}{DR} \gg 1$ for nearly two-dimensional motion.

All the theoretical work in bounded systems (eg Jacobs 1964, Stewartson 1967, Ingersoll 1969) supposes $\delta_L \gg 1$ but individual studies differ in the magnitude of $\delta_h$ and whether or not viscous effects are included or even dominate. By assuming $\delta_L \gg 1$ these studies exclude inertial wave radiation;

investigations including this effect are either in unbounded systems (Grace 1926 and Stewartson 1953) at zero Rossby number, or for shallow topography in bounded systems with small Rossby number (Cheng and Stewartson, 1979).

In the laboratory experiments involving flow visualisation, the discussion of the results and data has centred on the "Taylor column" phenomenon. In the present paper we suggest that the concept of a Taylor column has been applied with misleading generality and show that in some cases the flows are better understood in different terms. In particular we feel that the concept of a "leaning" Taylor column as introduced by Hide, Ibbetson and Lighthill (1968) could be reconsidered. Previous laboratory experiments not involving flow visulaisation but measuring the forces on an obstacle moving horizontally (Mason 1975 and 1977) concentrate on the parameter range of the "leaning" Taylor columns ($\delta_L \lesssim 1$, $\delta_h \lesssim 1$). In this range a drag force $\sim 2\Omega\rho UV$ (where $\rho$ is the fluid density and $V$ is the volume of the object) was observed and its dependence on the aspect ratios of cuboid objects was investigated. If A, B and C denote the lengths of the cuboids in the directions of $\underset{\sim}{U}$, $\underset{\sim}{U}\wedge\underset{\sim}{\Omega}$, and $\underset{\sim}{\Omega}$ respectively then for $C/\sqrt{AB} < 1$ the drag force was found to be $\sim 2\Omega\rho UBC^2$, whilst for $C/\sqrt{AB} \gtrsim 1$ the force was $\sim 0.5\,\Omega\rho UB^2C$. For all values of $C/\sqrt{AB}$ this result agreed with the theory of Stewartson (1953), who considered the motion of an ellipsoid in an unbounded inviscid fluid at zero Rossby number. The physical mechanism for Stewartson's drag is inertial wave radiation and Mason (1977) showed how linearised inertial wave drag theory accounted for the behaviour at $C/\sqrt{AB} \ll 1$. Further evidence of the importance of inertial waves in the parameter range of leaning Taylor columns is provided by the inviscid study of Cheng and Stewartson (1979), who show that the sloping disturbance is wavelike.

In the present paper we present some three-dimensional integrations of the Navier-Stokes equations for parameters of relevance to these laboratory experiments. Previous three-dimensional integrations by Huppert and Bryan (1976) were carried out for larger values of $\delta_L$ . The present integrations enable the flow patterns to be seen more clearly than the dye-wire techniques of the experimentalists. They confirm the conjecture that inertial wave radiation characterises the flow when $\delta_L \lesssim 1$ .

In the appendix to Hide Ibbetson and Lighthill (1968), Lighthill develops general ideas concerning inertial wave radiation and argues how this accounts for the leaning structure observed. His analysis leads to a slope associated with the leading edge of the main wave-like disturbance, but does not account for a Taylor column structure. His discussion is confirmed here, but the use of the term Taylor column for an essentially wave-like disturbance is misleading. In the laboratory experiments the wave-like character is partially hidden by the effects of viscosity which damp the waves within one or two wavelengths. These effects are seen most clearly in the numerical results but are also confirmed by some new experiments involving careful flow visualisation.

In § 2 we outline the numerical model and indicate the ranges of parameters accessible to it. The laboratory apparatus is described in § 3. In § 4 we present the numerical and experimental results and finally in § 5 the conclusions.

## 2. Numerical model

The equations of motion governing the integrations reported in this paper are the Navier-Stokes equations for an incompressible rotating fluid ie

$$\frac{\partial \underset{\sim}{u}}{\partial t} + \underset{\sim}{u}.\nabla \underset{\sim}{u} = -\nabla p + 2\underset{\sim}{\Omega}_{\wedge}(\underset{\sim}{u}-\underset{\sim}{u}_g) + \nu\nabla^2\underset{\sim}{u}$$

$$\nabla.\underset{\sim}{u} = 0$$

where $\underset{\sim}{u}=(u,v,w)$ is the velocity, $p$ is the perturbation dynamic pressure, $\nu$ is the kinematic viscosity, and $\underset{\sim}{\Omega}$ is the basic rotation. $\underset{\sim}{u}_g=(U,0,0)$ is the geostrophic wind, resulting from the background pressure gradient in the y-direction. The geometry and coordinate system are illustrated in Figure 1. The boundary conditions on the upper and lower surfaces are

$$\frac{\partial u}{\partial z} = \frac{\partial v}{\partial z} = w = 0 \qquad \text{on} \quad z = D$$

and

$$\underset{\sim}{u} = 0 \qquad \text{on} \quad z = h(x,y).$$

In both horizontal directions the domain of integration is taken to be periodic. The main reason for this choice, apart from its numerical simplicity, is the desire to avoid side-wall boundary layers requiring spatial resolution.

The numerical techniques we use to solve the equations have been discussed in Mason and Sykes (1978a and 1979) and will not be presented here. An important aspect of the numerical method concerns the approximate inclusion of the arbitrary no-slip surface $z = h(x,y)$. We use a cartesian mesh and, in order for the method (which involves making the viscous stresses continuous at $z = h(x,y)$) to be effectively second-order accurate, certain resolution requirements must be met. For the flows considered here with Rossby number $R \lesssim 1$ the errors incurred near the surface are $O(\Delta/\delta)$ (Mason and Sykes, 1978a) where $\Delta$ is the vertical mesh spacing and $\delta = (\nu/\Omega)^{1/2}$ is the depth of the Ekman boundary layer.

In practice we find the results to be essentially independent of $\Delta/\delta$ when $\Delta/\delta \lesssim 1/3$ . It follows that if, in the numerical model, we can dispose $n$ grid points up to the height $h_0$ of the topography, then $\delta$ must be $\gtrsim 3h_0/n$ . In the present work $n$ may be about 20 giving $\delta \gtrsim h_0/7$ . For Rossby numbers of unity and less this is the most stringent restriction on the model resolution. At larger Rossby numbers the dominant restriction is essentially an upper limit to the Reynolds numbers which may be considered. For small Rossby number flows the restriction on $\delta/h_0$ is only very severe for precisely those cases when a numerical model which parameterised the Ekman boundary layers (eg Vaziri and Boyer, 1971) would have utility. In this paper some results are obtained slightly beyond the area of efficient application of the method in order to illustrate the change in character of some flows seen in laboratory experiments.

## 3. Laboratory apparatus

The essential purpose of the apparatus was to tow an object mounted on a thin horizontal plate through a tank of fluid which was otherwise in solid body rotation. The fluid was contained in a rectangular tank mounted on a diameter of a turntable. The length of the tank was 1.20 m and the width and depth 0.20 m. The depth of the working fluid was generally less than the depth of the tank and the upper surface to the fluid was free. The axis of the turntable was vertical to within $10^{-4}$ radians and values of angular rotation speed $\Omega$ were in the range 0.5 to 1.0 rad $s^{-1}$ and constant to within 0.01%. The main errors in the experiment arose from spurious convection currents present in the fluid. These were minimised by extensive thermal insulation and the use of a thin film of oil on the upper surface of the fluid to prevent evaporation. The fluid was either water or, when a higher viscosity was desired, a water-glycerol mixture. The final magnitude of the background motions were $\sim 0.01$ cm $s^{-1}$. The thin horizontal plate had thickness 3 mm and was suspended from a framework by rods of 5 mm diameter mounted close to the edges of the tank. The objects used were sufficiently small for them to be effectively isolated from effects due to these rods and the sidewalls. The plate was long enough for the initial flow effects involving the formation of Ekman boundary layers to have subsided. This meant that the Rossby number based on the length of the plate had to be small. The other effect of the plate was a deflection of the flow through the mechanism of vortex compression (eg Batchelor

1967 p573). At smaller Rossby numbers than those for which data is presented, this effect necessitated the use of a thinner horizontal plate. As discussed in Mason (1975), effects due to the parabolic shape of the free upper surface of the liquid should be negligible.

The flow visualisation was achieved by means of the well known Baker (1966) technique employing the p.H. indicator thymal blue. Wires generating the p.H. change were mounted upstream of the objects, from the frame work supporting the horizontal plate. Two 35 mm cameras were attached to the moving framework to photograph from above and from the side.

## 4. Results

In all the results presented, both numerical and experimental, we have adopted a standard form of topography. We have chosen a smoothly-shaped obstacle to avoid both separation effects from sharp edges in the laboratory studies, and also numerical problems near sharp corners in the integrations. The height of the topography is

$$h = h_0 \cos^2\left[\frac{\pi}{2L}(x^2+y^2)^{\frac{1}{2}}\right] \quad \text{for} \quad x^2+y^2 < L^2,$$

$h=0$ for $x^2+y^2 \geq L^2$. The relative size of the computational domain was $10L$ in the x-direction and $7.5L$ in the y-direction. This was large enough to effectively isolate the topography.

### (a) Inertial wave regime

First we illustrate a flow typical of a so-called leaning Taylor column. A laboratory and a numerical experiment have been performed with the same basic parameters; these are given in Table 1 case A. Ignoring factors of order $\pi$, $\delta_L$ is the ratio of the vertical wavelength of inertial waves with horizontal scale $L$ to the depth of the container. Thus here when $\delta_L = 2$ we expect to see three-dimensional motion characterised by inertial waves.

Figure 2 shows a comparison between the experimental dye observations and the numerical results. Starting at the upstream coordinates of the vertical dye-generation wire, trajectories have been computed from the steady-state numerical velocity field (by the method described in Mason and Sykes, 1979) and superimposed onto a photograph of the experimental dye release. The comparison is difficult because although the initial coordinates are upstream of the centre of the obstacle in both sets of trajectories, small spurious motions in the experiment cause the dye to shift sideways slightly, into

different parts of the velocity field, with consequent increasing errors. By calculating trajectories using the numerical results from different initial positions, it has been ascertained that errors due to the spurious lateral displacements in the laboratory study are typically of the same magnitude as the differences visible in the comparison. However it is clear that there is good agreement in the character of the flow. The disturbance decays both with height and in the downstream direction. Fig 3 shows the computed horizontal velocity vectors and vertical velocity field a few Ekman layer depths above the top of the obstacle while Fig 4 shows the same fields at $z = D/2$. The wave-like character of the flow is evident and the horizontal fields show the transverse motion of the inertial waves. For comparison we have made a calculation based on the inviscid linearised theory of Queney (1947) (see appendix to Mason (1977) for details), and Fig 5 shows the resulting vertical velocity field at a height comparable with the numerical results in Fig 4b. 128 x 128 points have been used for the numerical Fourier analysis of the topography in the linear theory, using the same horizontal domain as the Navier-Stokes model and the results are essentially independent of resolution. Fig 5 shows finer scale details than could be expected in the viscous numerical integration. The waves also extend much further around the domain, but near to the obstacle the phase of the disturbance is similar to that observed. Better agreement away from the obstacle cannot be expected, since the results from the Navier-Stokes equations are clearly dominated by viscous effects in this region.

Hide, Ibbetson and Lighthill (1968) measured the slope of the position of maximum upward displacement of their dye. This slope of the "leaning" Taylor columns was found to be $1.54R$, where $R$

is the Rossby numer based on the diameter of their spherical object. This value of slope would not be expected to be in quantitative agreement with that arising from an obstacle of difference shape, as used in this study. For the numerical integration, the slope was measured as 1.3R, where the length scale in the Rossby number, $U/\Omega L$, is the base radius. Linear, inviscid theory also provides a means of estimating the slope of the disturbance, but owing to dispersive effects, the leading edge of the wavelike disturbance is not quite a straight line. Notwithstanding this difficulty, the linear theory prediction is in agreement with the Navier-Stokes result to within about 20%. Ideally, the Navier-Stokes result should be compared with the bounded, inviscid theory of Cheng and Stewartson (1979), but the dominant effects of viscosity in our results limit the usefulness of such a calculation.

The above results clearly show how inertial waves account for the main features of this type of flow. The influence of inertial wave radiation on the force acting the topography is discussed below.

(b) Two-dimensional flow regime

In this section we illustrate two examples (B and C) of two-dimensional flows which occur when $\delta_L \gg 1$. The parameters involved are given in Table 1. In example B, viscous and inertial effects are comparable. The ratio of the spin-up time of the flow to the advection time $E^{1/2}/R = 1.88$, cf. 0.14 in the inertial wave example in which internal dissipation was also important. Fig 6 shows the horizontal velocity vectors a few boundary layer scales above the obstacle and Fig 7 shows the vertical velocity fields at the same height (7d) and about half way up the domain (7b). From Fig 6 it is clear that $\delta_h$ is not large enough for the flow to be completely blocked, though strong deflection with much diminished flow above obstacle is evident. Fig 7a and b give a clear indication of the almost complete two-dimensionality of the flow. For comparison with previous results and with the experiments cited below, Fig 8 shows a view from above of some flow trajectories. These show the same features as Fig 6. In Fig 9 we present limiting surface streamlines projected onto a horizontal plane (see Mason and Sykes (1979) for computational details). These are fairly close to the interior flow pattern when allowance is made for the $45^\circ$ shift between stress and basic flow direction due to the Ekman boundary layer.

In example C the horizontal flows are almost the same as in example B and are not presented but some extra features can be seen in the vertical velocity field. In example C, $\delta_h$ is larger but viscous effects dominate; $E^{1/2}/R = 8.32$. The vertical velocity field in Fig 10 shows more "twisting up" of the regions of ascent and descent over the obstacle and in the lee two positive contours can be seen. This is due to the vorticity

of the fluid which descends from the obstacle. When the fluid filaments ascend the obstacle they are compressed and acquire negative vorticity much of which is then lost though spin-up. Thus on descending from the obstacle and stretching, the filaments then acquire positive vorticity.

Whilst the latter examples are of interest in giving the full Navier-Stokes equation solution for those flows, similar results can be obtained from two-dimensional equations based on the assumption $\delta_L \gg 1$ as would be expected from the observed two-dimensionality. Vaziri and Boyer (1971) have made a numerical study of these equations and compared the result with experiments. The examples B and C presented here have parameter ratios falling between those depicted in Fig 5(b) and (c) of Vaziri and Boyer.

Forces

In the homogeneous fluid considered here we expect a drag force resulting from inertial wave radiation (and subsequent viscous dissipation) and also from viscous dissipation of the standing disturbance produced by the obstacle. In Mason and Sykes (1978b) the forces involved in flow over small amplitude topography for $\delta_h \ll 1$ and $\delta_l \gg 1$ are considered. Due to the linearity of the Ekman boundary layer equations the surface stress is proportional to the mean velocity in the interior. Since the motion is essentially two-dimensional, the continuity equation implies the average of the mean velocity, and thus the average viscous stress, is unchanged. The force due to viscous dissipation arises from Ekman boundary layer pumping dissipating the disturbance due to the obstacle. In the examples considered here the assumption $\delta_h \ll 1$ and $\delta_l \gg 1$ are never met and magnitude of the drag due to viscous dissipation is difficult to estimate. However the general grounds upon which the mean viscous stress was expected to be unchanged should apply. In Table 2 the net viscous forces on the domain with and without the obstacle are given and this result is confirmed.

The drag due to inertial waves was considered in detail by Mason (1975 and 1977). In accordance with his conclusions in example A we find the value of drag given by the inviscid linearised theory is in fair agreement with computed values of pressure force in the x-direction. The perturbation pressure force on the obstacle also has a component in the y-direction; this is in the opposite direction to the force due to the geostrophic pressure gradient, which has magnitude $2\Omega\rho U V$, where $V$ is the volume of the obstacle, and acts in the positive y-direction. The linear theory, in which the

flow is symmetric about the x-axis, gives no such force (cf Figures 5 and 4b). In the case of a complete Taylor column, $\delta_L >> 1$ and $\delta_h >> 1$, this y-direction perturbation pressure force has magnitude $2\Omega\rho UV$, producing zero net force in the y-direction when the background component is added. Mason (1975) argued that the approach of this perturbation force from zero to $2\Omega\rho UV$ could be taken as a measure of the approach towards a Taylor column flow. When scaled by $2\Omega\rho UV$ the perturbation y-direction forces in cases B and C are very similar. This follows from the prevously noted similarity in flow patterns between these cases. The values of the y (and x) direction forces in these cases are fairly similar to those obtained for spheres in laboratory experiments (see Mason 1975 Fig 6). The x-force in these cases may contain a contribution from inertial wave radiation but the main cause is the viscous dissipation due to the Ekman layers which was mentioned above.

## 5. Conclusions

We have shown the utility of a numerical model in studying rapidly rotating flow over topography. The integrations have confirmed previous conjectures by showing how the "leaning" Taylor column flow which occurs when $R < 1$ and $\delta_L \leq 1$ can be largely described in terms of inertial waves. When $R \ll 1$ and $\delta_L > 1$ the flow outside the boundary layers is seen to be two-dimensional and accords well with models based on the stricter assumption, $R \ll 1$, $h_o \ll D$.

## 6. Acknowledgements

The authors wish to express their gratitude to Mr. W.D.N.Jackson who built the experimental apparatus and conducted the laboratory experiments.

## References


Bachelor, G.K. 1967 'An introduction to fluid dynamics' Cambridge University Press.

Baker. D.J. 1966 'A technique for the precise measurement of small fluid velocities'. J. Fluid Mech. 26, 573-576.

Cheng, H.K. and Stewartson, K. 1979 'On the structure of inertial waves produced by an obstacle in a deep, rotating container'. To appear in J. Fluid. Mech.

Grace, S.F. 1926 'On the motion of a sphere in a rotating liquid'. Proc. Roy. Soc. A 113, 46-47.

Hide, R. 1961 'Origin of Jupiter's Great Red Spot'. Nature, 190, 213-218.

Hide, R., Ibbetson, A. & Lighthill, M.J. 1968 'On slow transverse flow past obstacles in a rapidly rotating fluid'. J. Fluid Mech. 32, 251-272.

Huppert, H.E. and Bryan, R. 1976 'Topographically generated eddies'. Deep Sea Res. 23, 655-679.

Ingersoll, A.P. 1969 'Inertial Taylor columns and Jupiter's Great Red Spot'. J. Atmos. Sci. 26, 744.

Jacobs, S.J. 1964 'The Taylor column problem'. J. Fluid Mech. 20, 581-591.

Mason, P.J. 1975 'Forces on bodies moving transversely through a rotating fluid'. J. Fluid Mech. 71, 577-599.

Mason, P.J. 1977 'Forces on spheres moving horizontally in a rotating stratified fluid'. Geosphys. Astrophys. Fluid Dynamics. 8, 137-154.

Mason, P.J. and Sykes, R.I. 1978a 'A simple Cartesian model of boundary layer flow over topography'. J. Comp. Phys. 28, 198-210.

Mason, P.J. and Sykes, R.I. 1978b 'On the interaction of topography and Ekman boundary layer pumping in a stratified atmosphere'. Quart. J. Roy. Met. Soc. 104, 475-490.

Mason, P.J. and Sykes, R.I. 1979 'Three-dimensional numerical integrations of the Navier-Stokes equations for flow over surface mounted obstacles'. To appear in J. Fluid Mech.

Proudman, J. 1916 'On the motions of solids in a liquid possessing vorticity'. Proc. Roy. Soc. A92, 408-424.

Queney, P. 1947 'The problem of air flow over mountains: a summary of theoretical studies'. Bull. Am. Meteor. Soc. 29, 16-26.

Stewartson, K. 1953 'On the slow motion of an ellipsoid in a rotating fluid'. Quart. J. Mech. Appl. Math. 6, 141-162.

Stewartson, K. 1967 'On slow transverse motion of a sphere through a rotating fluid'. J. Fluid Mech. 30, 357-369

Taylor, G.I. 1923 'Experiments on the motion of solid bodies in rotating fluids'. Proc. Roy. Soc. A104, 213-218.

Vaziri, A. and Boyer, D.L. 1971 'Rotating flow over shallow topographies'. J. Fluid Mech. 50, 79-95.

Figure 1

Illustrating the domain of the Navier-Stokes equation integrations.

Figure 2

Superposition of experimental dye traces and computed trajectories from the numerical integration of case A. (See Table 1).

Figure 3

Results obtained from the numerical integration of case A. Horizontal sections at a height $z = h_0 + 3\delta$, where $\delta = (\nu/\Omega)^{1/2}$. (a) horizontal velocity vectors (b) vertical velocity field. The contour interval is $0.015 cms^{-1}$ and the dashed lines denote negative values.

Figure 4

Results obtained from the numerical integration of case A. Horizontal sections at a height $z = D/2$. (a) horizontal velocity vectors (b) vertical velocity field. The contour interval is $0.008\ cm\ s^{-1}$ and the dashed lines denotes negative values.

Figure 5

Prediction of linear theory for basic parameters corresponding to case A. A horizontal section of the vertical velocity field at a height $z = D/2$ is shown. The contour interval is $0.02\ cm\ s^{-1}$ and the dashed lines denote negative values.

Figure 6

Results obtained from the numerical integration of case B. Horizontal velocity vectors at $z = h_0 + 3\delta$ where $\delta = (\nu/\Omega)^{1/2}$.

Figure 7

Results obtained from the numerical integration of case B. Horizontal sections of vertical velocity field at (a) $z = h_0 + 3\delta$, and (b) $z = D/2$. The contour intervals are $1.7 \times 10^{-3}$ and $1.3 \times 10^{-3}\ cm\ s^{-1}$ respectively; dashed lines denote negative values.

Figure 8

A projection onto a horizontal plane of computed flow trajectories at $z=D/2$ in case B.

Figure 9

A projection on to a horizontal plane of computed limiting $(z \to h(x,y))$ streamlines for case B.

Figure 10

Results obtained from the numerical integration of case C. Horizontal section of the vertical velocity field at $z = h_o + 3\delta$. The contour interval is $8\times10^{-4}\,cms^{-1}$ and dashed lines denote negative values.

Table 1 : Basic parameters

| Case | A | B | C |
|---|---|---|---|
| Dimensional parameters | | | |
| $\Omega$ / rad $s^{-1}$ | 0.5 | 1.0 | 2.0 |
| $L$ / cm | 2 | 2 | 4 |
| $h_o$ / cm | 2 | 1 | 2 |
| $D$ / cm | 20 | 3 | 6 |
| $U$ / cm | 0.2 | 0.1 | 0.1 |
| $\nu$ / $cm^2$ $s^{-1}$ | 0.02 | 0.01 | 0.1 |
| dimensionless parameters | | | |
| $R = U/4\Omega L$ | 0.05 | 0.012 | 0.003 |
| $E^{1/2} = (\nu/2\Omega D^2)^{\frac{1}{2}}$ | $7.1\ 10^{-3}$ | $2.4\ 10^{-2}$ | $2.6\ 10^{-2}$ |
| $E^{1/2}/R$ | 0.14 | 1.19 | 8.3 |
| $\delta_h = h_o/DR$ | 2 | 27 | 107 |
| $\delta_L = L/DR$ | 2 | 53 | 213 |

Table 2 Net forces in MKS units

| Case | A | B | C |
|---|---|---|---|
| undisturbed viscous force | | | |
| in x direction | $6.53\ 10^{-8}$ | | $5.55\ 10^{-7}$ |
| in y direction | $5.27\ 10^{-8}$ | | $5.16\ 10^{-7}$ |
| Final viscous force | | | |
| in x direction | $6.48\ 10^{-8}$ | $3.11\ 10^{-8}$ | $5.54\ 10^{-7}$ |
| in y direction | $5.26\ 10^{-8}$ | $2.85\ 10^{-8}$ | $5.13\ 10^{-7}$ |
| Perturbation pressure force on obstacle | | | |
| in x direction | $6.0 \pm 0.5\ 10^{-9}$ | $2.5 \pm 0.01\ 10^{-9}$ | $4.2 \pm 0.2\ 10^{-8}$ |
| in y direction | $3.5 \pm 0.2\ 10^{-9}$ | $4.9 \pm 0.01\ 10^{-9}$ | $8.8 \pm 0.2\ 10^{-8}$ |
| Calculated pressure force in x direction due to linearised inertial wave radiation. | $9.9 \times 10^{-9}$ | - | - |
| Perturbation Pressure force on obstacle scaled by $2\ell_0 UV$ | | | |
| in x direction | 0.40 | 0.35 | 0.35 |
| in y direction | 0.23 | 0.68 | 0.74 |

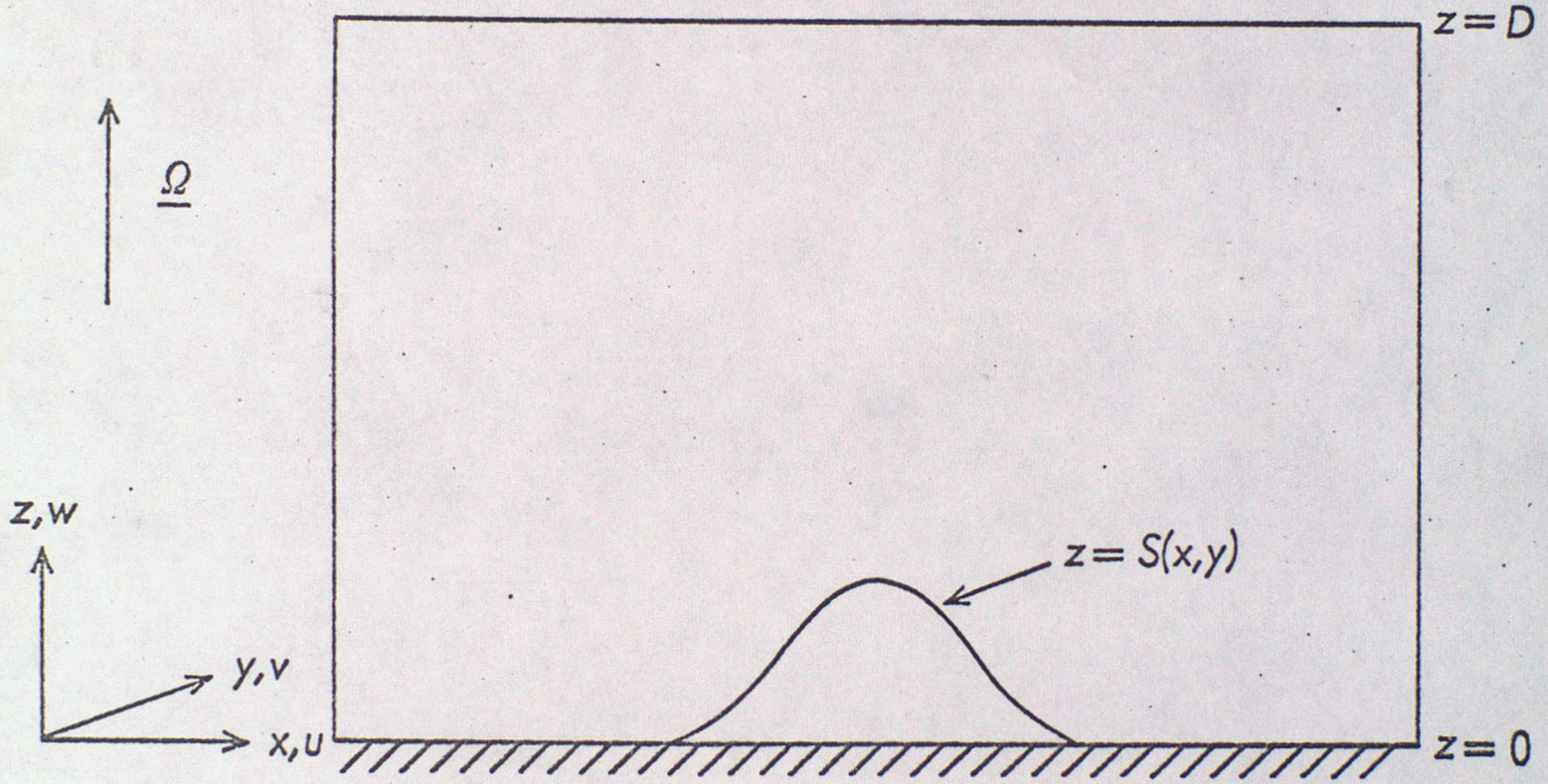


fig 1

Fig 8

Fig 3a-b

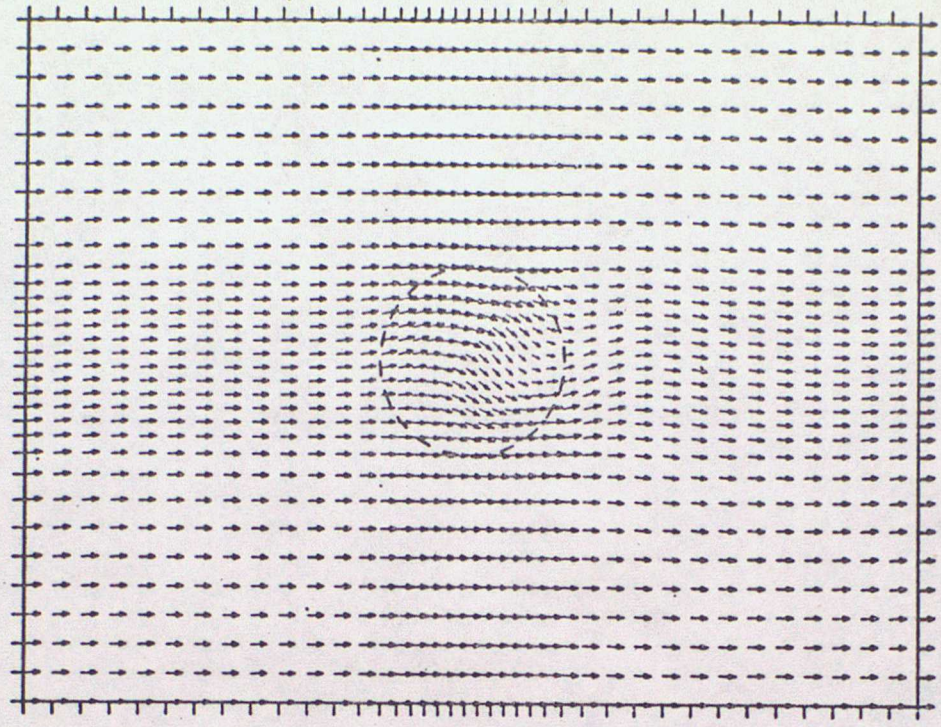

Fig 3a

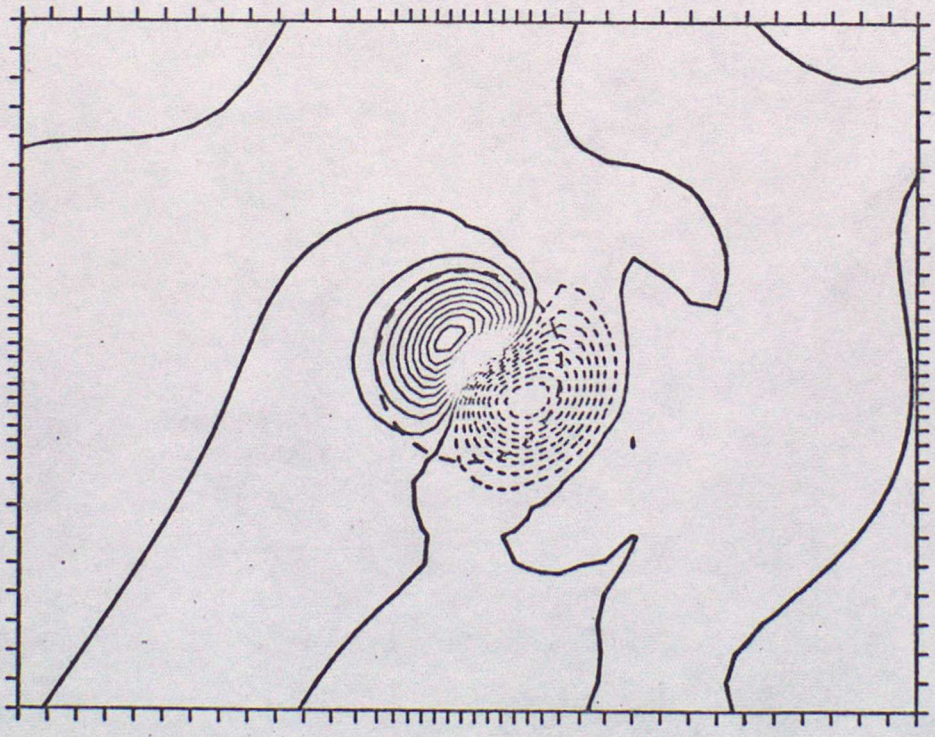

Fig 3b

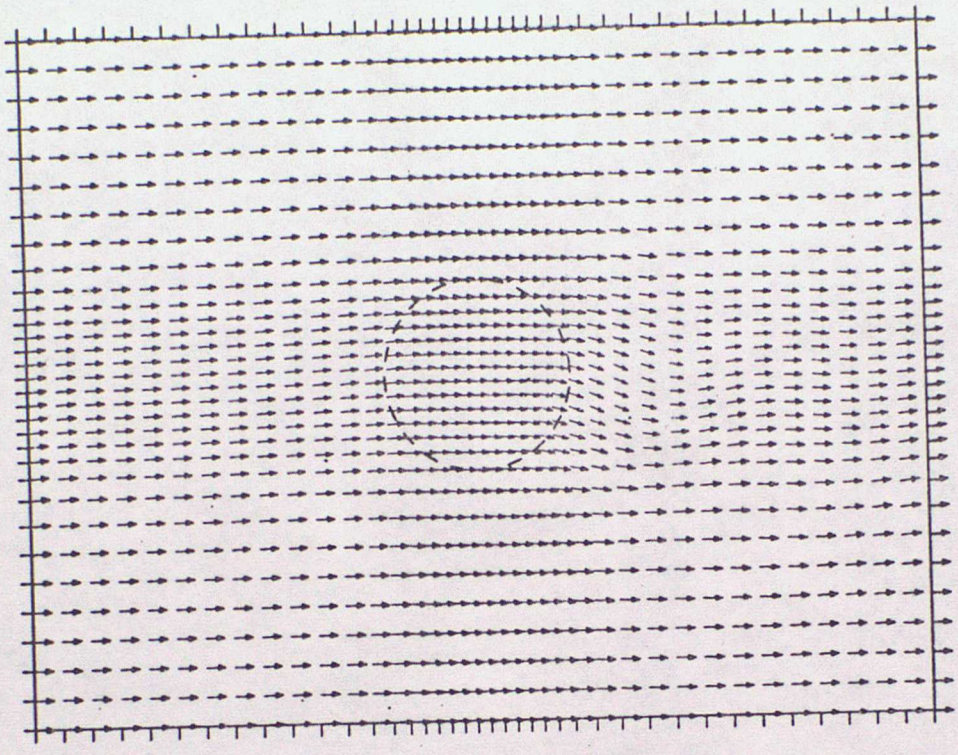

Fig 4a

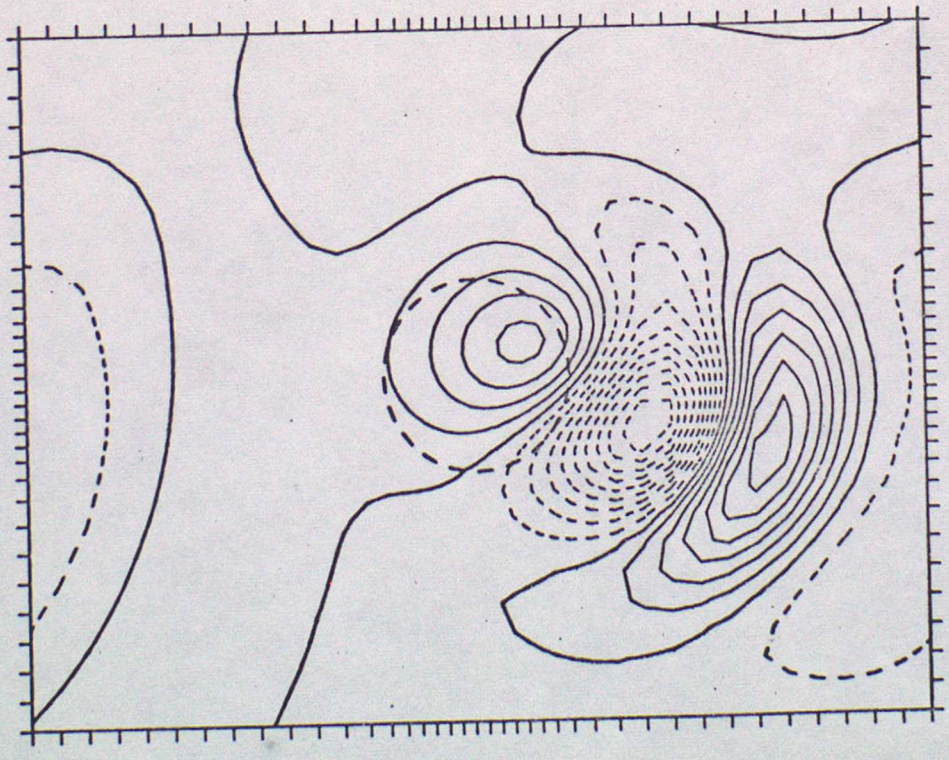

Fig 4b

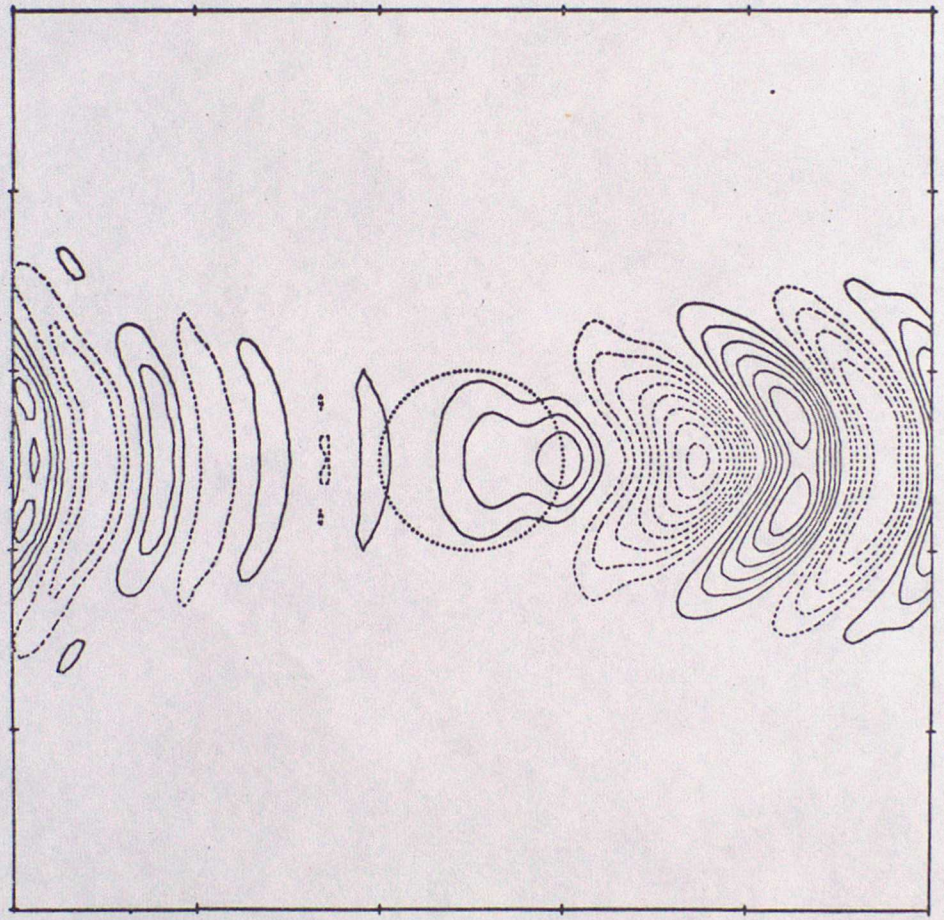

Fig 5

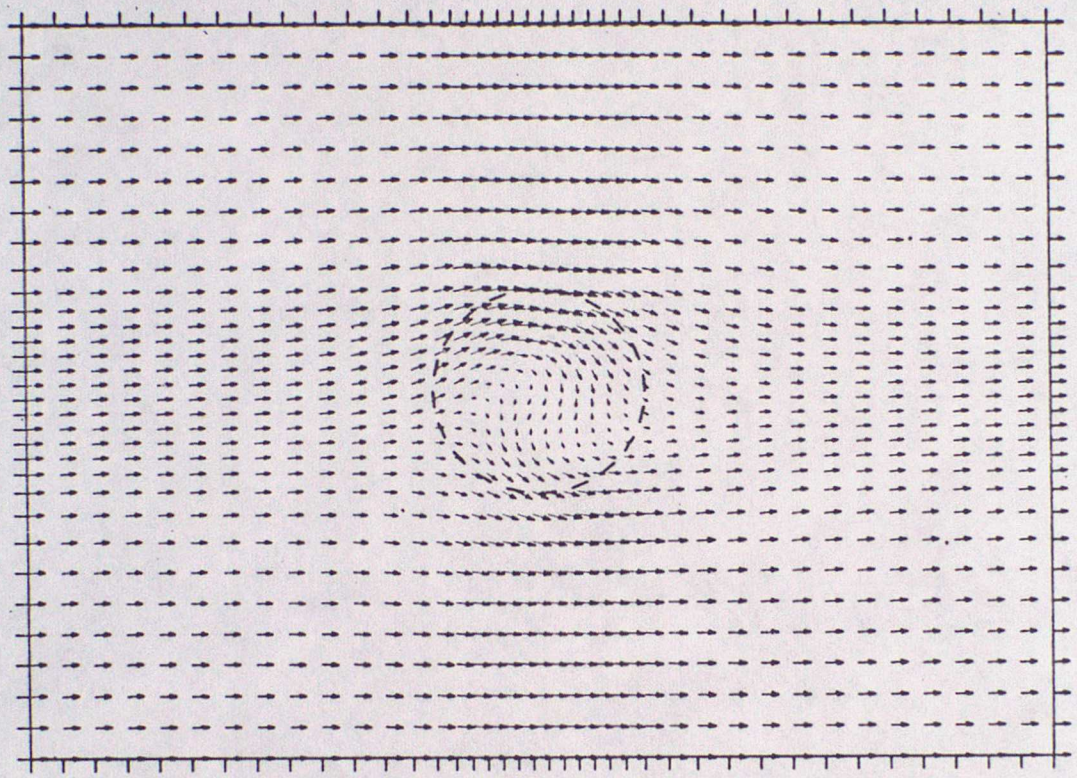

Fig 6

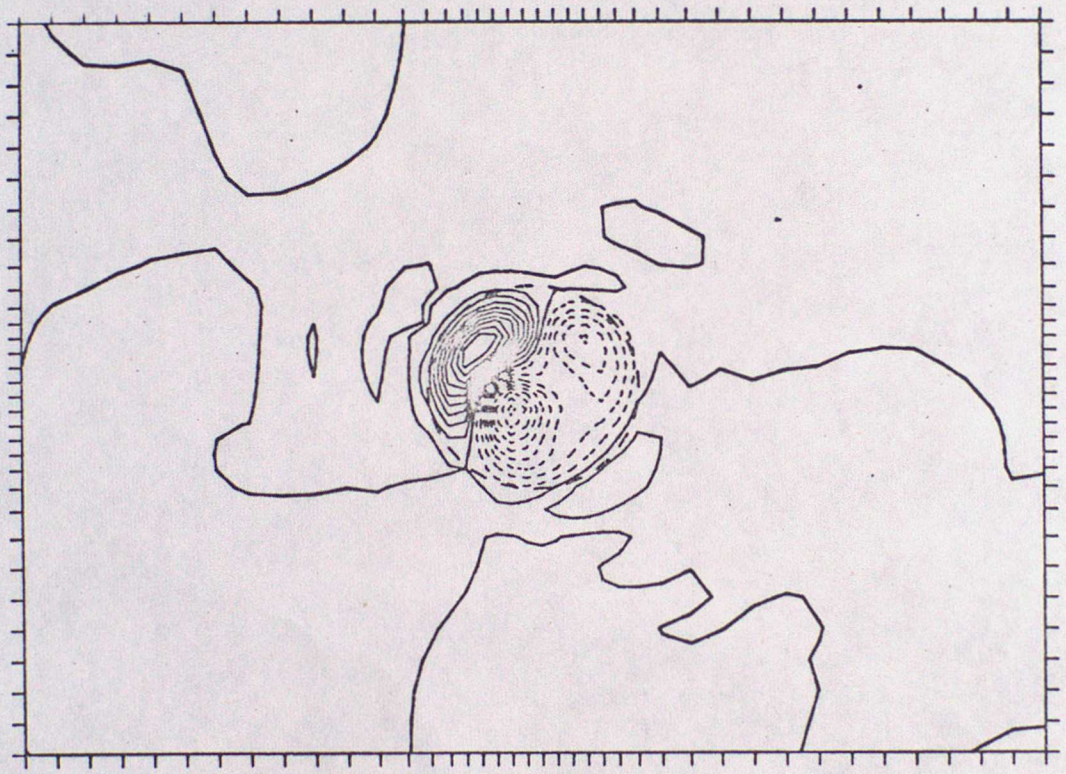

Fig 7a

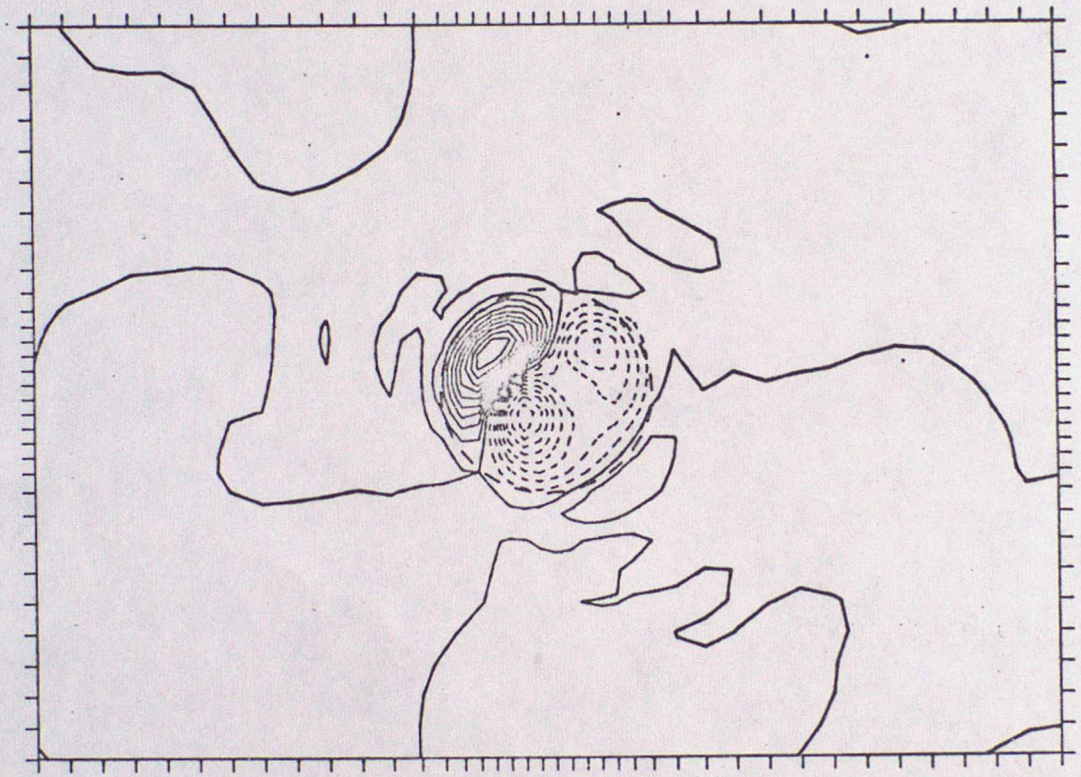

Fig 7b

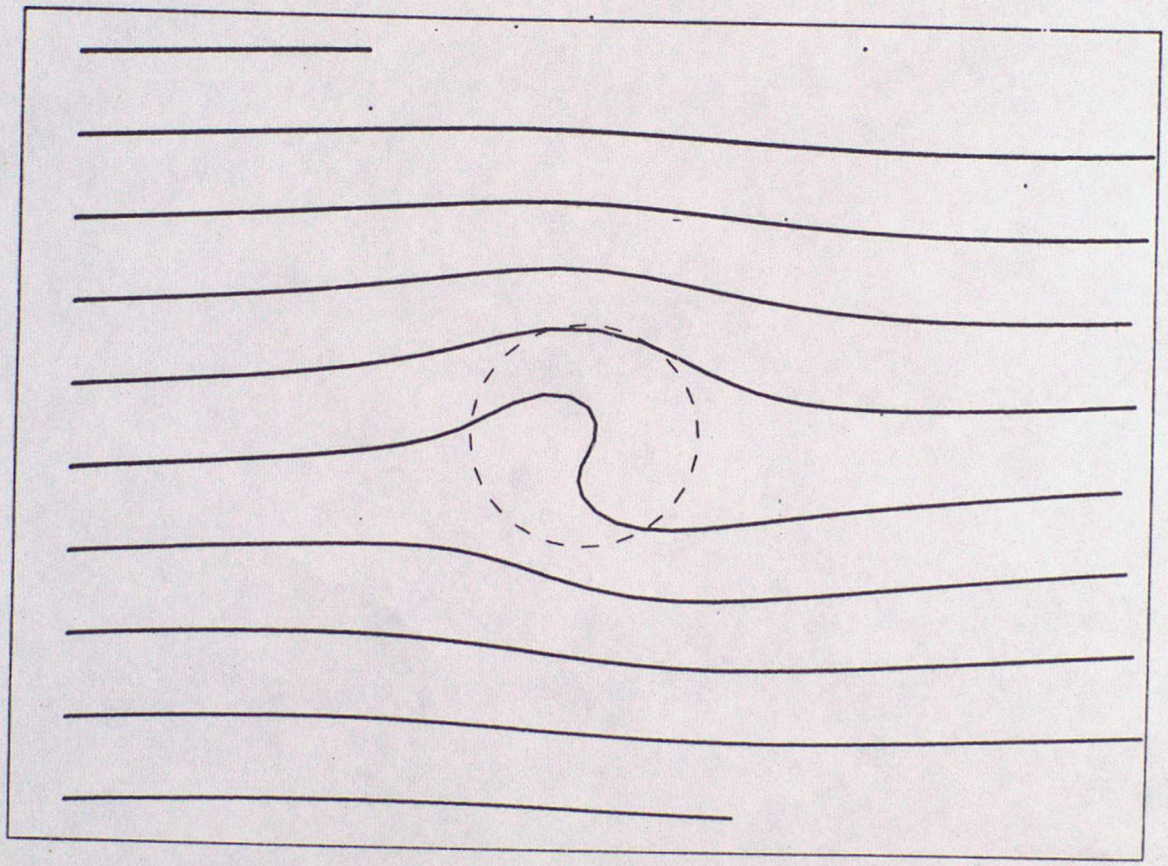

Fig 8

fig 9

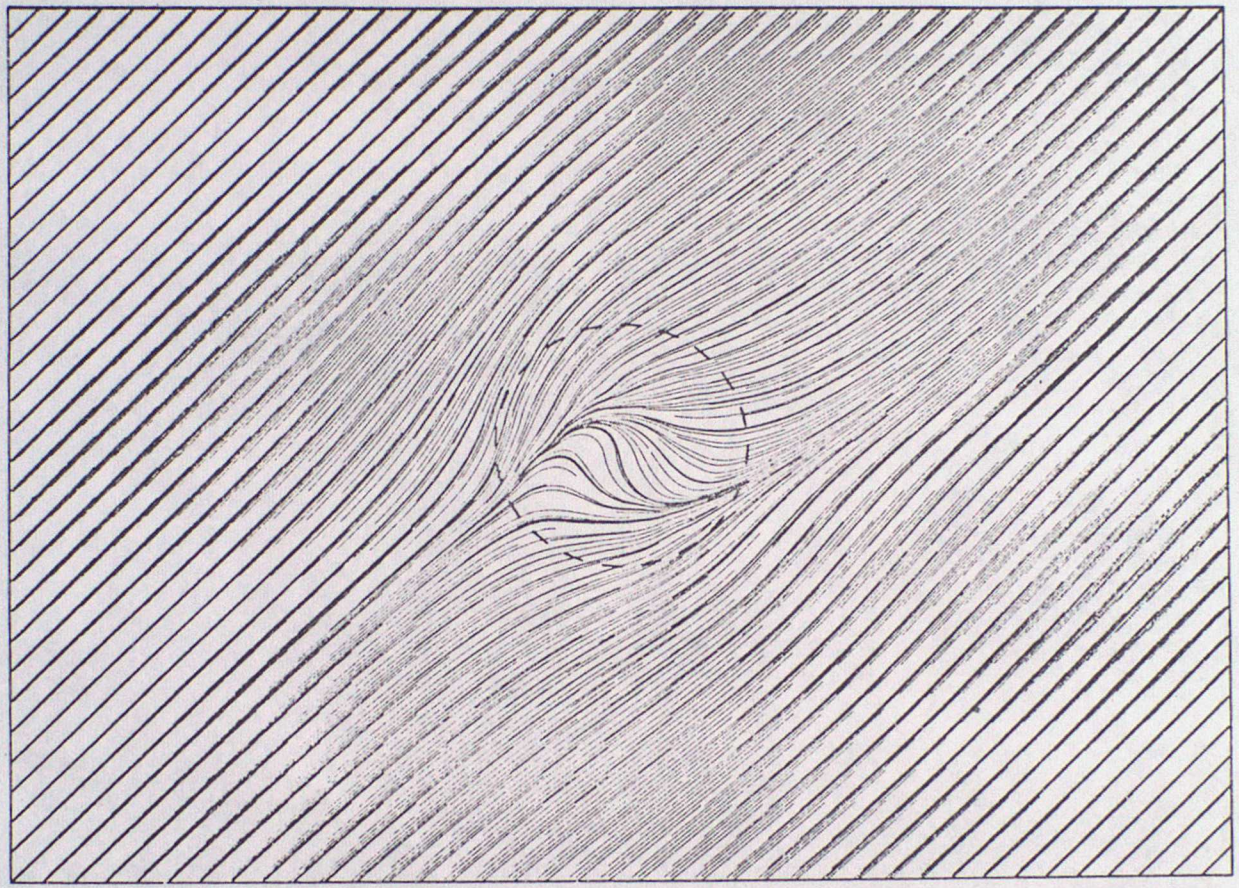

fig 9

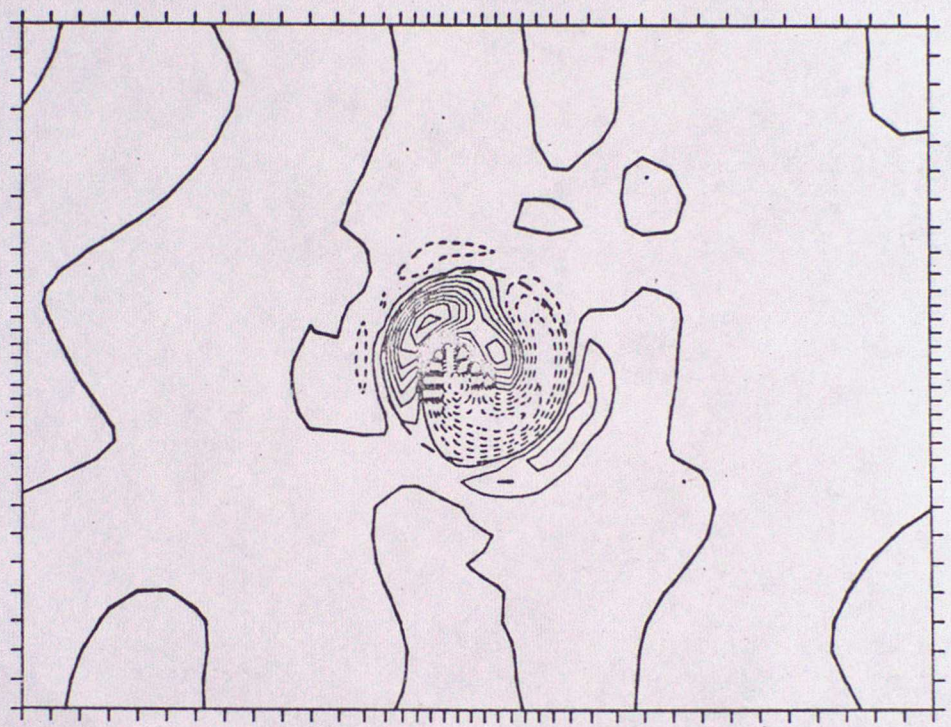

Fig 10